Korean Chem. Eng. Res., 57(3), 425-431 (2019)
https://doi.org/10.9713/kcer.2019.57.3.425
PISSN 0304-128X, EISSN 2233-9558

Development of Micro-Tubular Perovskite Cathode Catalyst with Bi-Functionality on ORR/OER for Metal-Air Battery Applications

Yukwon Jeon*,,†, Ohchan Kwon**, Yunseong Ji**, Ok Sung Jeon**, Chanmin Lee*** and Yong-Gun Shul**,†**

**School of chemistry, University of St Andrews, Fife, KY16 9ST, United Kingdom*
***Department of Chemical and Biomolecular Engineering, Yonsei University, Yonsei-ro 50, Seodaemun-gu, Seoul, 03722, Korea*
****Research Institute of Sustainable Manufacturing System, Intelligent Sustainable Materials R&D Group, Korea Institute of Industrial Technology (KITECH), 89 Yangdaegiro-gil, Ipjang-myeon, Seobuk-gu, Cheonan-si, Chungcheongnam-do, 31056, Korea*
(Received 6 March 2019: accepted 3 April 2019)

Abstract – As rechargeable metal-air batteries will be ideal energy storage devices in the future, an active cathode electrocatalyst is required with bi-functionality on both oxygen reduction reaction (ORR) and oxygen evolution reaction (OER) during discharge and charge, respectively. Here, a class of perovskite cathode catalyst with a micro-tubular structure has been developed by controlling bi-functionality from different Ru and Ni dopant ratios. A micro-tubular structure is achieved by the activated carbon fiber (ACF) templating method, which provides uniform size and shape. At the perovskite formula of $LaCrO_3$, the dual dopant system is successfully synthesized with a perfect incorporation into the single perovskite structure. The chemical oxidation states for each Ni and Ru also confirm the partial substitution to B-site of Cr without any changes in the major perovskite structure. From the electrochemical measurements, the micro-tubular feature reveals much more efficient catalytic activity on ORR and OER, comparing to the grain catalyst with same perovskite composition. By changing the Ru and Ni ratio, the $LaCr_{0.8}Ru_{0.1}Ni_{0.1}O_3$ micro-tubular catalyst exhibits great bi-functionality, especially on ORR, with low metal loading, which is comparable to the commercial catalyst of Pt and Ir. This advanced catalytic property on the micro-tubular structure and Ru/Ni synergy effect at the perovskite material may provide a new direction for the next-generation cathode catalyst in metal-air battery system.

Key words: Metal-air battery, Cathode catalyst, Perovskite, Micro-tubular, Bi-functionality

1. Introduction

Through the continuous battery development, the battery market has been wider throughout our society. In recent years, although the secondary battery, mainly lithium ion battery, has been used as a main power sources for mobile phone, notebook, and automobile, new battery systems have been under study due to the limitations of long-term use and charging depending on locations [1-3]. Among many, metal-air battery technology is considered as a next-generation energy supply. The metal-air battery runs by the oxidation reaction at the metal (anode), and by the reduction reaction at the catalyst material (usually, Pt-Ir/C) using air as a reactant (cathode), which is a sort of fuel cell system [4-6]. The most common forms are lithium-air, zinc-air, and aluminum-air, etc., which have different energy density/voltage and operating conditions [7-12]. Metal-air batteries do not discharge environmental pollutants and can be constructed to many types by relatively low cost [13-14]. And the O_2 is constantly supplied from air as an energy source, which provides stable voltage until the metal is oxidized.

† To whom correspondence should be addressed.
E-mail: yj24@st-andrews.ac.uk, shulyg@yonsei.ac.kr
‡This article is dedicated to Prof. Yong-Gun Shul on the occasion of his retirement from Yonsei University.

However, some problems are still remained such as battery stability and sensitivity to the external environment, limited output characteristics, temperature range, metal corrosion, and electrolyte loss etc. [15-18]. Particularly, one of the most problems that hinder its further commercialization into the marketplace is the use of expensive cathode catalysts. The metal-air battery operates in aqueous solutions by electrochemical reactions of oxygen reduction reaction (ORR) and oxygen evolution reaction (OER) during discharge and charge, respectively. However, most of the metal-air batteries suffer from the sluggish kinetic during the ORR/OER cycling, which causes large voltage gap during the cycles and poor power capability [19-21]. Noble metal catalysts such as Pt, Pd for ORR and Ir for OER, have been considered due to the high reactivity, but the high costs and shortage block their widespread use in large-scale applications [22,23]. Therefore, new approaches such as metal oxides and carbon-based materials, have been investigated and designed to achieve bi-functionality on ORR/OER with high activity and stability for the use as a cathode materials in metal-air battery systems.

Perovskite structured materials, general formula of ABO_3, have been known as a good catalyst in such kind of oxygen involved reactions (ORR/OER) due to its high oxygen ion mobility and chemical/structural stability [24,25]. Moreover, the cations in A and B can be selected according to the reaction conditions. Meanwhile, the compound of $LaCrO_3$ has been widely studied as an electrode catalyst material owing to its chemical and structural stability [26]. Gener-

ally, the B cation is known to be responsible for the catalytic activity, where partial substitution provides structural changes in the valence state and non-stoichiometry-related defects to improve the catalytic activity and conductivity of the catalyst [27-29]. Therefore, the high oxygen ion transfer property from the rearrangement of the lattice structure and the catalytic properties of the dopant can make a synergetic reaction mechanism of the perovskite catalyst for an efficient ORR/OER with relatively lower cost. Tailoring the morphology and surface structure of the perovskite have been received a great interest in the field of catalysis and electrochemistry [30,31]. Especially, unique properties of the fibrous perovskites are reported, such as high geometrical surface area to allow for a high dispersion of the active phase, high volumetric density, short diffusion distance for better mass/charge transfer and flexibility with endless geometric forms, which are effective on various applications in catalysis and even electrochemistry fields [32-34].

In an effort to develop an effective bi-functional electrocatalyst for rechargeable metal-air battery, we designed micro-tubular perovskite cathode catalysts based on $LaCrO_3$ with a partial dual substitution in the lattice. To design a bi-functionality at the perovskite material, Ru and Ni dopant were applied due to these well-known ORR and OER activities, respectively. The micro-tubular perovskite materials with different Ru and Ni compositions were synthesized by the ACF template method to produce a micro-tubular feature. The positive effect on the micro-tubular shape at catalytic reactions was seen from the ORR and OER activity in comparison with the grain perovskite. By changing the Ru/Ni ratio, the structural difference of the perovskites was investigated and their catalytic bi-functional properties toward ORR and OER were explored in an aqueous alkaline electrolyte.

2. Experimental Section

2-1. Synthesis of perovskite micro-tubular materials

The $LaCrO_3$ based micro-tubular materials were synthesized by following procedure of the ACF (activated carbon fiber) templating method from our previous work [31,32]. An aqueous (solution) impregnation synthesis on ACF were used due to its rapid and convenient process to produce high surface area oxides. The ACF templates were treated in acid solutions of H_2SO_4 (6 M) and HNO_3 (6 M) to remove surface impurities and to functionalize the ACF surface. The calculated stoichiometric solutions of $La(NO_3)_3{\cdot}9H_2O$, $Cr(NO_3)_3{\cdot}9H_2O$, $Ni(NO_3)_3{\cdot}6H_2O$, and $HN_4O_{10}Ru$ were used in water base. The prepared ACF was immersed for 24 hours in the solutions of a certain stoichiometric La^{III}, Cr^{III}, Ni^{III}, and Ru^{III} ions to ionically bond the metal cations to the negatively charged carbon surface. After 24 hours drying, the samples were heat-treated at a mild condition of 1027 K for 6 hours in sufficient air flow for the C content combustion and formation of crystalline structure at the same time. Finally, the $LaCr_{1-(x+y)}Ru_xNi_yO_3$ perovskite hollow fibers: (x=0.15, y=0.05), (x=0.1, y=0.1) and (x=0.05, y=0.15) were obtained with the Ru/Ni loadings of 10.37/1.14 wt%, 7.79/2.34 wt% and 4.00/3.61 wt%, respectively. For comparison, $LaCr_{1-(x+y)}Ru_xNi_yO_3$ perovskite grain with (x=0.05, y=0.15) is prepared by the same procedure by using AC (activated carbon) template.

2-2. Characterization

The micro-tubular structure of the prepared samples was observed by using scanning electron microscope (SEM) operated at 15 kV in JSM-6701F (JEOL). Moreover, high-resolution transmission electron microscopy (HR-TEM) images were collected at 200 kV in JEM-2100F (JEOL). For the perovskite crystal structure analysis, X-ray diffraction (XRD) was performed by Rigaku Miniflex AD11605 with X-ray diffractometer using Cu Kα radiation (λ = 1.5405 nm) at 30 kV and 30 mA. The X-ray absorption spectroscopy (XAS) spectra were recorded in Pohang Accelerator Laboratory (PAL, South Korea). The X-ray absorption near edge structure (XANES) data of Ni $L_{3,2}$-edge and Ru $M_{3,2}$-edge were collected at beamline 10D XAFS (Bending magnet, Phoibos 150). Measurements were made at room temperature using thin layers of solid powder samples deposited on transparent adhesive tape. For comparison, all the spectra were calibrated by first measuring the spectrum of NiO and RuO_2, respectively.

2-3. Electrochemical experiments

To evaluate the electrocatalytic activity, rotating disc electrode (RDE) experiments were carried out by setting on the Rotate Assembly Instructions (Pine Instruments) with a three-electrode cell system. A potentiostat (VSP, BioLogic) was used for the electrochemical measurements. To prepare the catalyst ink, 1 mg conductive carbon (Vulcan XC72R) + catalyst (carbon: catalyst = 6:4) was dispersed in 1 ml EtOH and 80 ul of Nafion solution (5 wt.% in lower aliphatic alcohols and water, 1100 EW). The catalyst ink was ultra-sonicated for 1 hour for homogeneous mixing. The suspension was dropped onto a glass carbon electrode (ϕ = 5 mm) and dried at room temperature in ambient air until the catalyst distributed uniformly across the electrode surface. The electrochemical evaluation of each catalysts was performed by linear sweep voltammetry (LSV) for the oxygen reduction reaction (ORR) and oxygen evolution reaction (OER) measurements. At the electrolyte of 6 mol KOH, Pt wire and Hg/HgO electrode (1 mol NaOH) were used as the counter and reference electrodes, respectively. Before starting each measurement, the electrolyte was bubbled with high-purity O_2 for 30 min, and maintained during the measurement for the O_2-saturated condition. LSV curves for both ORR and OER were collected from -0.25 to 0.95 V vs. Hg/HgO at the scan rate of 5 mV/s and RDE rotation speed of 1600 rpm. For comparison, commercial catalyst of 40% Pt-Ir (1:1 atomic ratio) on Vulcan XC-72 (Premetek Co.) was measured at the same condition.

3. Results and Discussion

3-1. Micro-tubular perovskite material

To synthesize micro-tubular perovskites doped with a dual system

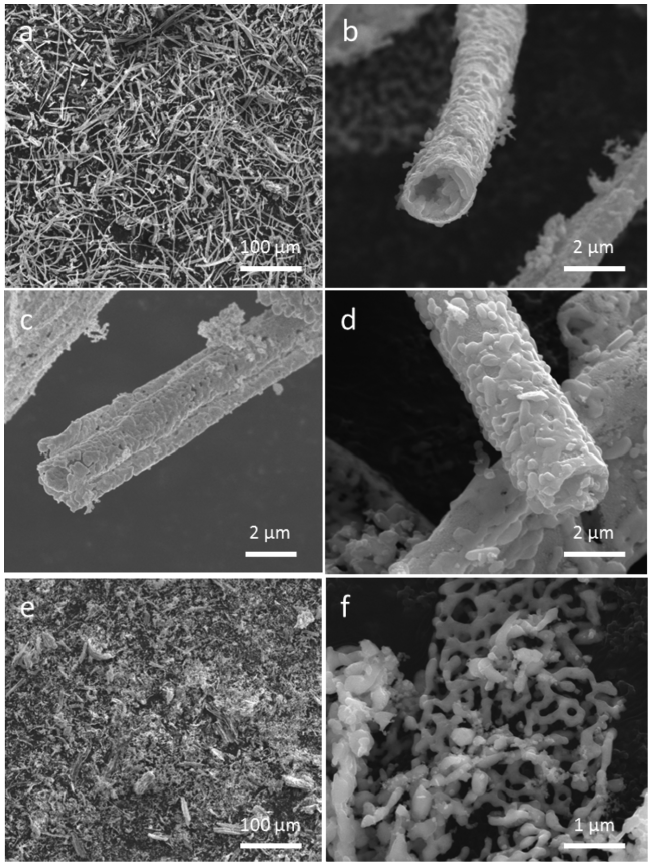

Fig. 1. (a) SEM images for the $LaCr_{1-(x+y)}Ru_xNi_yO_3$ perovskite micro-tubulars: (b) x=0.15, y=0.05, (c) x=0.1, y=0.1 and (d) x=0.05, y=0.15, and (e-f) $LaCr_{1-(x+y)}Ru_xNi_yO_3$ (x=0.05, y=0.15) grain perovskite.

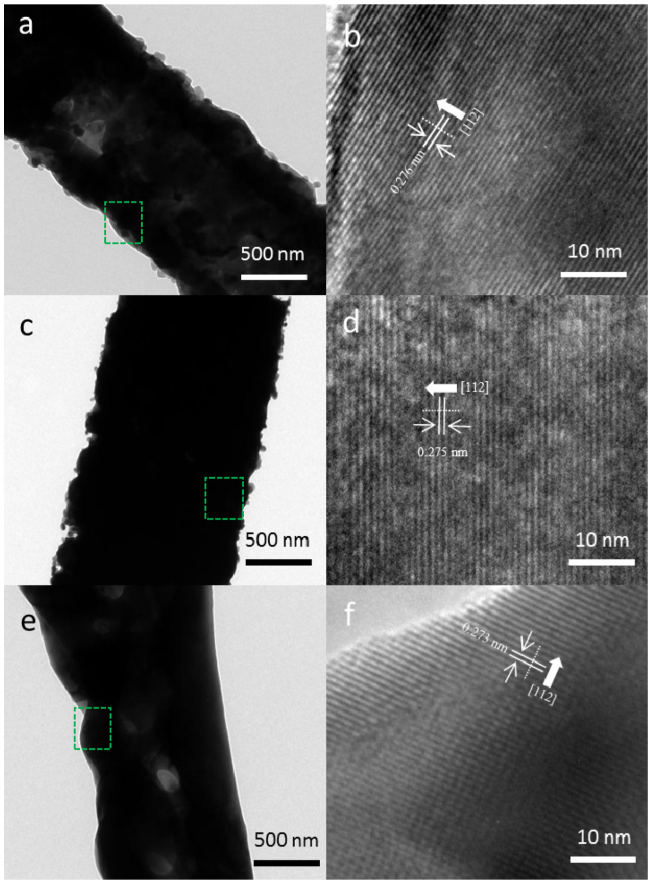

Fig. 2. TEM images for the $LaCr_{1-(x+y)}Ru_xNi_yO_3$ perovskite micro-tubulars: (a-b) x=0.15, y=0.05, (c-d) x=0.1, y=0.1 and (e-f) x=0.05, y=0.15.

of Ru and Ni, carefully calculated $La^{III}Cr^{III}_{1-(x+y)}Ru^{III}_xNi^{III}_y$ stoichiometric compositions were loaded on an acid-treated ACF, and then heat-treated at 1027 K under air flow to combust the carbon content and synthesize perovskites. From the SEM images in Fig. 1(a)-(d), perfect micro-tubular structures were achieved with the perovskite networks of $LaCr_{1-(x+y)}Ru_xNi_yO_3$ (x=0.15, y=0.05), (x=0.1, y=0.1) and (x=0.05, y=0.15). The diameter and length of the micro-tubulars are obviously uniform with the outer and inner fiber diameters in the ranges of 0.8~1.4 μm and 1.7~2.1 μm, respectively. The length/diameter ratio was also over 70, which corresponds well to a fibrous structure (Fig. 1(a)). This micro-tubular feature was previously reported to provide large specific surface area and unique pore structure comparing to the non-templated and even AC templated perovskites [32]. In Figure 1(e)-(f), the morphology of the perovskite using AC template shows random size and shape of their grains. Comparing the surface structure of the fibrous perovskites, it was interesting that we could observe a slight difference in the sizes of the perovskite grains connected to the micro-tubular feature, depending on the Ru and Ni ratio. The perovskite with higher Ru doping level revealed rougher surface by less sintering (Fig. 1(b)-(c)) than the Ni-rich perovskites (Fig. 1(d)), confirming a lower sintering effect by the substitution of Ru that might provide more efficient activity.

Fig. 2 displays the TEM analysis of the prepared perovskite catalysts. A noticeable micro-tubular structure can be found from the TEM images (Fig. 2(a),(c),(e)), which are matched with the shape and size at the SEM images. Furthermore, the dark contrast of the micro fibers can be recognised with the highly interconnected grains that has a single perovskite phase. From the magnified area in each microfiber edges (Fig. 2(b),(d),(f)), highly crystalline structures were observed with certain interplanar distances. The interplanar distances varied by 0.276 nm, 0.275 and 0.273 nm for the $LaCr_{1-(x+y)}Ru_xNi_yO_3$ perovskites with (x=0.15, y=0.05), (x=0.1, y=0.1) and (x=0.05, y=0.15), respectively, depending on the ionic size of the dopant in the perovskite structure.

3-2. Structural analysis of the perovskites

The structural difference of the $LaCr_{1-(x+y)}Ru_xNi_yO_3$ perovskites with (x=0.15, y=0.05), (x=0.1, y=0.1) and (x=0.05, y=0.15) can be confirmed by the XRD analysis, which is shown in Fig. 3. According to the results, homogeneous and highly crystalline XRD patterns were obtained with the main perovskite diffraction peaks. The (hkl) indices were assigned to (110)/(002), (112)/(020), (202)/(022), (220)/(004), (114), (024), and (224)/(040), which exactly matched to the orthorhombic structure of $LaCrO_3$ within the *Pbnm* space group

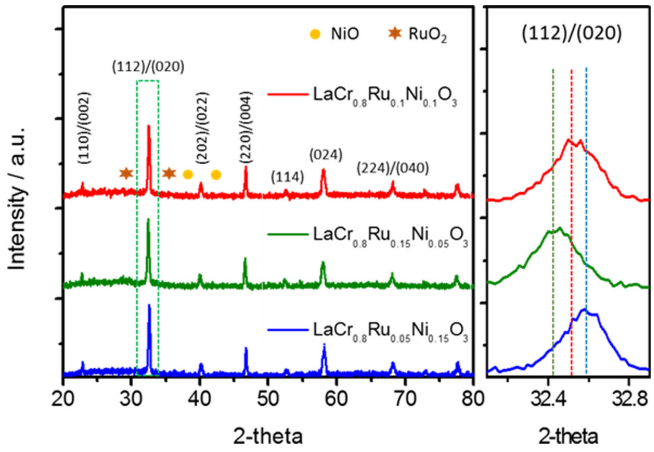

Fig. 3. XRD patterns and evolution of phases of the $LaCr_{1-(x+y)}Ru_xNi_yO_3$ perovskite micro-tubulars: (x=0.15, y=0.05), (x=0.1, y=0.1) and (x=0.05, y=0.15), with inset for the magnified XRD patterns.

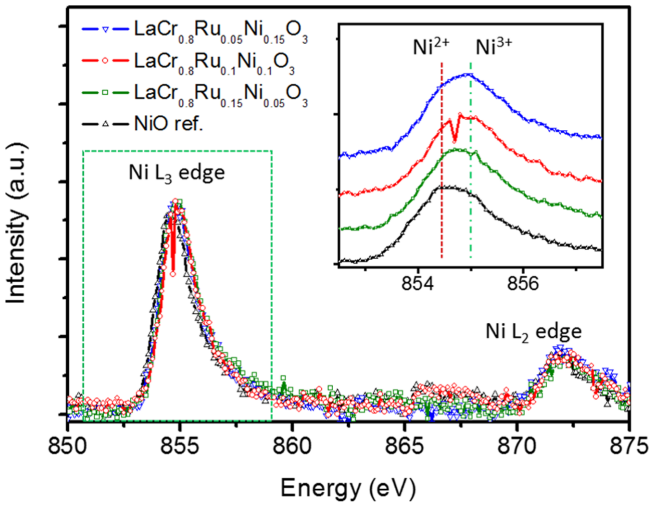

Fig. 4. The normalized XANES spectra of Ni $L_{3,2}$-edge of the $LaCr_{1-(x+y)}Ru_xNi_yO_3$ perovskite micro-tubulars: (x=0.15, y=0.05), (x=0.1, y=0.1) and (x=0.05, y=0.15), with inset for the magnified XANES spectra.

reported in powder diffraction file JCPDF 024-1016 [35]. This confirms that the Ru and Ni are perfectly incorporated in the lattice structure without any change in the original perovskite structure. Another evidence of the full substitutions is the invisible NiO and RuO_2 peaks in each XRD patterns, which confirms also single perovskite phases. However, the doped perovskite structures can be slightly distorted from the different bonding lengths to the neighbouring oxygen atoms. From the magnified image of the (112)/(020) reflection at the right-hand side in Fig. 3, the incorporation of Ru and Ni in the $LaCrO_3$ perovskite structure caused peak displacement to different angles depending on the size and ratio of the dopants. Also, different basal spacings are revealed from the d-values of 2.763 Å, 2.761 Å and 2.758 Å for the $LaCr_{1-(x+y)}Ru_xNi_yO_3$ perovskites with (x=0.15, y=0.05), (x=0.1, y=0.1) and (x=0.05, y=0.15), respectively, which shows a similar trend with the interplanar distances at the TEM results (Fig. 2) and our previous work [31]. From these results, it was obvious that the different crystal ionic radii of Ru^{III} (0.820 Å) and Ni^{III} (0.700 Å) attributed to this slight change by the partial substitution with Cr^{III} (0.755 Å) at the B-site.

To investigate the chemical structure, the chemical oxidation states of the $LaCr_{1-(x+y)}Ru_xNi_yO_3$ perovskites were also investigated by the X-ray absorption near edge structure (XANES), as shown in Fig. 4 and 5. Generally, the oxidation states of elements are determined by the X-ray photoemission spectroscopy (XPS) that is a sensitive and straightforward technique. However, XPS measurements suffered from a charging effect, causing shifts by the influence of the electron energy [36]. In addition, XPS only measures the sample surface in very thin depth. In the case of the XANES analysis, the energy was defined by incident radiation, which can avoid spectra shift from the charging effect [37,38]. Therefore, XANES technique can be more adequate to specify the valence state of Ni and Ru in our study.

Ni $L_{3,2}$-edge XANES spectra for the prepared perovskites that was substituted by Ni with different doping level was shown in Fig. 4, including NiO as a reference. Comparing both L_3 and L_2 edges, all spectra shows the typical peak with some changes in the shape and position due to the different oxidation states in each structure. From dipole selection rule, the Ni $L_{3,2}$-edge XANES spectra explains a transition from Ni 2p→3d states [37]. Therefore, the total number of empty 3d states at Ni sites can be directly confirmed by the integrated intensity of each $L_{3,2}$-edge peaks. Basically, the NiO reference represents the Ni ion with a formal valance of Ni^{2+}. As can be seen in the inset of Fig. 4, the peaks at the L_3-edges for the Ni species in the perovskite structure became much broader and shifted to the higher energies. And, this trend was more obvious at the perovskites with higher Ni doping level. Recorded data suggest that the majority of Ni ions are in Ni^{3+} state with a slight contribution of Ni^{2+} or maybe Ni^{4+}. This confirms a perfect Ni incorporation into the perovskite structure and we can similarly explain the Ru incorporation by the analysis of Ru $M_{3,2}$-edge XANES spectra.

Fig. 5 displays the Ru $M_{3,2}$-edge XANES spectra for the perovskites that was substituted by Ru with different doping level, and RuO_2 as a reference. The absorption of M_3-edge is at around 465 eV where the core electrons at Ru $3p_{3/2}$ absorb photons at 460-470 eV [39]. So, the electron yield signals for our samples indicate the transition from $3p_{3/2}$ to 4d for both t_{2g} and e_g. Since the M_2-edge is smaller due to the smaller number of j=1/2 states and the transfer from $3p_{1/2}$ to 4d is forbidden, M_3-edge is mainly used to clarify the oxidation states from the ratio of empty t_{2g} and e_g bands. The XANES spectra for RuO_2 is used as a reference with a formal valance of Ru^{4+}. Based on this, we can see that the Ru species incorporated in the perovskite structure changed to a higher valance states from the shifts to the higher energy. Interestingly, the Ru energy levels of the samples with the higher Ru doping split to two obvious peaks, which implies a mixed valence of Ru^{4+} and Ru^{5+}. This feature is from the cubic crystal field effect due to the edge-sharing RuO_6 octahedral configuration [32,40]. Therefore, it strongly suggests a stabilized local symmetry

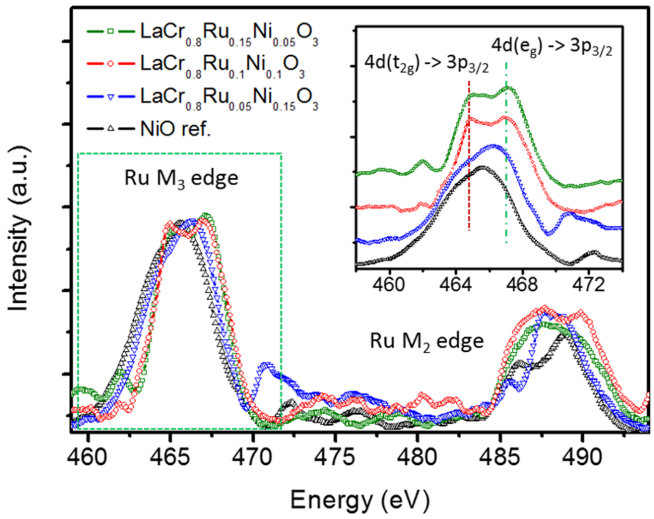

Fig. 5. The normalized XANES spectra of Ru $L_{3,2}$-edge of the $LaCr_{1-(x+y)}Ru_xNi_yO_3$ perovskite micro-tubulars: (x=0.15, y=0.05), (x=0.1, y=0.1) and (x=0.05, y=0.15), with inset for the magnified XANES spectra.

for Ru, nearly regular octahedral symmetry at the orthorhombic lattice, along with the Ni in the dual doping system in $LaCr_{1-(x+y)}Ru_xNi_yO_3$.

3-3. Electrocatalytic activity of the micro-tubular perovskites

To examine the electrocatalytic capability as a cathode material in the metal-air battery system, the electrochemical behaviors of the prepared micro-tubular perovskites towards ORR and OER were evaluated by LSV using RDE experiments in the half cell set-up. All samples were mixed with carbon black as a conducting agent and Nafion as a binder. The mixtures were uniformly coated onto an RDE electrode for a fine electrochemical measurement in 6 mol KOH solution using a standard three-electrode system with an Hg/HgO reference electrode. Meanwhile, due to the RDE tests with 1600 rpm, the influence of oxygen transport on the evaluation of the catalytic activities could be negligible.

Fig. 6 demonstrates a better activity of the micro-tubular perovskite structure for both ORR and OER comparing to the grain catalyst when the perovskite compositions were fixed. Focusing on the ORR region in the polorisation curve, it was clearly seen that the micro-tubular structure shows almost two time higher current density with the values of 0.44 and 0.66 mA/cm^2 (grain: 0.25 and 0.33 mA/cm^2) at the half-wave and limiting potentials, respectively. A similar trend was seen for the steeper slope of the micro-tubular perovskite catalyst at the OER region by even wider difference with the current density values of 1.11 and 2.65 mA/cm^2 (grain: 1.75 and 0.87 mA/cm^2) at the half-wave and limiting potentials, respectively. From these better bi-functional activity, it is obvious that the micro tubular feature provides advantages to use as an electrode material due to the large surface-to-volume ratio and surface areas highly exposed to the surrounding environment. Furthermore, the fibrous structure can have more open pores with an increased number of triple phase boundary (TPB) sites where the catalyst, reactant and conducting material meet together for an efficient electrochemical reaction [33,34]. Therefore, these advantages can result in enhanced electrochemical activity, and maybe even better durability for the metal-air battery system.

To control the bi-functionality of the micro-tubular perovskite catalysts, the ratios of Ru and Ni were varied at the perovskite formula of $LaCr_{1-(x+y)}Ru_xNi_yO_3$ with (x=0.15, y=0.05), (x=0.1, y=0.1) and (x=0.05, y=0.15). The prepared perovskite catalysts were tested for electrochemical ORR and OER in 1M KOH solutions. On the anodic branch for OER in Fig. 7, an excellent OER activity was achieved by the perovskite catalyst that possesses the highest Ni doping level in the structure. This value is still lower than the commercial catalyst (40% Pt-Ir), but it can be seen comparable due to the relatively low Ni loading of 3.61 wt% and total metal (Ru+Ni) loading of 7.61 wt%. We could see that the current density value for the OER activity increases in square from 0.19 and 0.82 mA/cm^2 to 1.12 and 2.65 mA/

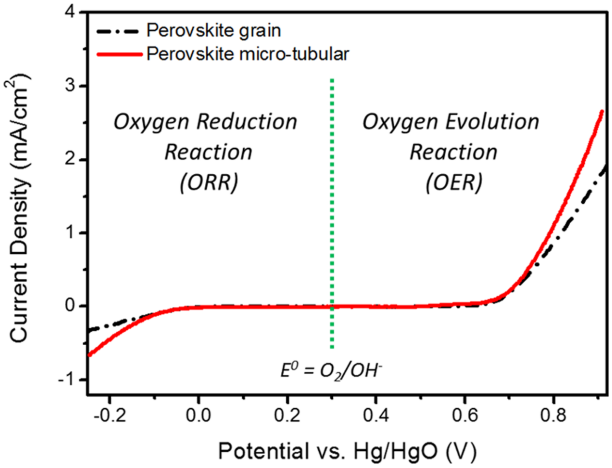

Fig. 6. ORR and OER polarization curves of the grain and micro-tubular $LaCr_{1-(x+y)}Ru_xNi_yO_3$ perovskite with (x=0.05, y=0.15) at the measurement condition of -0.25 to 0.95 V vs. Hg/HgO with the scan rate of 5 mV/s and RDE rotation speed of 1600 rpm in the O_2-saturated 6 mol KOH.

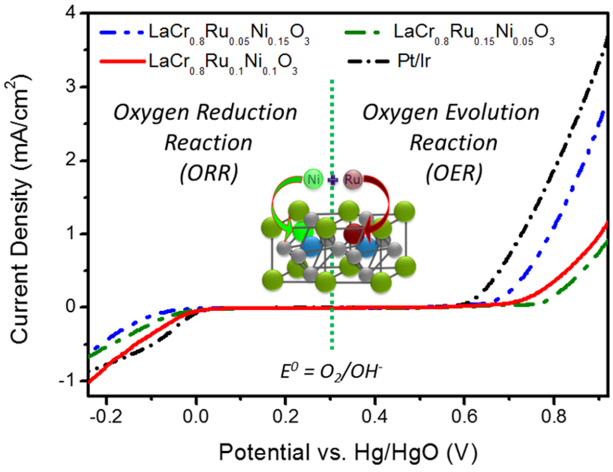

Fig. 7. ORR and OER polarization curves of the micro-tubular $LaCr_{1-(x+y)}Ru_xNi_yO_3$ perovskite: (x=0.15, y=0.05), (x=0.1, y=0.1) and (x=0.05, y=0.15), at the measurement condition of -0.25 to 0.95 V vs. Hg/HgO with the scan rate of 5 mV/s and RDE rotation speed of 1600 rpm in the O_2-saturated 6 mol KOH.

cm^2 at the half-wave and limiting potentials, respectively, following the order of Ni^{3+} proportion that was confirmed in the XANES analysis. We can say that the OER activity is not only related to the Ni doping amount due to the preferential electronic structure of Ni for OER but also the higher valence state of Ni with the oxygen structure at the perovskite, which can more easily adsorb OH^- for an efficient oxygen evolution.

In addition to the requirement of high OER activity, catalytic materials for rechargeable metal-air batteries should be able to effectively catalyze electrochemical oxygen reduction, which is of particular importance for improving their reversible efficiency. From the cathodic region for ORR in Fig. 7, a reasonable result was seen comparing the opposite Ru/Ni ratio of $LaCr_{1-(x+y)}Ru_xNi_yO_3$ with (x=0.15, y=0.05) and (x=0.05, y=0.15). As Ru is known as a ORR catalyst, the perovskite catalyst with more Ru shows higher activity with the current density values of 0.22 and 0.71 mA/cm^2 than the other (0.12 and 0.66 mA/cm^2) at the half-wave and limiting potentials, respectively. As doped perovskites are generally known to have oxygen defects which strongly involves in the oxygen related reactions, the higher activity can be also from the more obvious edge-sharing RuO_6 octahedral configuration at the perovskite. Interestingly, the perovskite composition of $LaCr_{0.8}Ru_{0.1}Ni_{0.1}O_3$ shows the best ORR activity with the current density values of 0.37 mA/cm^2 at the half-wave potential. The limiting current density of 1.01 mA/cm^2 was even higher than the commercial catalyst (0.87 mA/cm^2, Pt+Ir=40 wt%) at a very low Ru (7.79 wt%) and total metal (Ru+Ni=10.13 wt%) loadings. In this case, we can assume that there is a Ru and Ni synergy effect on ORR under a sufficient Ru loading that has mixed valance of RuO_6 octahedral configuration. Moreover, the great limiting current density can be also from the micro-tubular feature which we discussed before. At the same time, the $LaCr_{0.8}Ru_{0.1}Ni_{0.1}O_3$ shows also a reasonable OER activity with the current density values of 0.37 and 1.04 mA/cm^2 at the half-wave and limiting potentials, respectively. Even though the catalytic activity, especially OER has to be more enhanced, we can insist that the micro-tubular perovskite catalyst of $LaCr_{0.8}Ru_{0.1}Ni_{0.1}O_3$ has a good bi-functionality on ORR and OER at a low metal loading.

4. Conclusions

Herein, we designed a micro-tubular perovskite catalyst with a dual dopant system of Ru and Ni to achieve a bi-functionality on ORR and OER for the metal-air battery applications. The preparation of unique micro-tubular was introduced by the means of ACF template, which provides high surface area and open pore structure in the electrode for efficient mass transfer property. From the physiochemical characterizations, the formation of a micro-tubular structure was confirmed. The Ru and Ni dopants were finely incorporated in the perovskite lattice in any ratios, which was studied from the crystallography and X-ray spectroscopy analysis. The micro-tubular perovskite catalyst shows higher activity than the grain due to its better catalytic availability. We found also that a bi-functionality on ORR and OER can be tuned by the different Ru and Ni dopant ratio. The metal alloy synergy effect enhanced the catalytic activity at certain Ru and Ni composition, which was confirmed from the comparable bifunctional activity of the micro-tubular perovskite catalyst of $LaCr_{0.8}Ru_{0.1}Ni_{0.1}O_3$ to the commercial catalyst at the relatively lower metal loading. This approach on micro-tubular structure and bi-functionality control should be applicable not only to metal-air battery systems but also to many other catalytic and electrochemical applications.

Acknowledgements

This article is dedicated to the Professor Yong-gun Shul, who is retiring in 2019. We would like to express our sincere respect and gratitude to his exceptional contributions towards the study of catalysis and Fuel cells.

Reference

1. Blurton, K. F. and Sammells, A. F., "Metal/air Batteries: Their Status and Potential - a Review," *J. Power Sources*, **4**, 263-279 (1979).
2. Zhang, X., Wang, X.-G., Xie, Z. and Zhou, Z., "Recent Progress in Rechargeable Alkali Metal-air Batteries," *Green Energy & Environment*, **1**, 4-17(2016).
3. Li, Y. and Lu, J., "Metal-air Batteries: Will They Be the Future Electrochemical Energy Storage Device of Choice," *ACS Energy Lett.*, **2**(6), 1370-1377(2017).
4. Wang, Z.-L., Xu, D., Xu, J.-J. and Zhang, X.-B., "Oxygen Electrocatalysts in Metal-Air Batteries: from Aqueous to Nonaqueous Electrolytes," *Chem. Soc. Rev.*, **43**, 7746-7786(2014).
5. Cheng, F. and Chen, J., "Metal-air Batteries: From Oxygen Reduction Electrochemistry to Cathode Catalysts," *Chem. Soc. Rev.*, **41**, 2172-2192(2012).
6. Li, Y., Gong, M., Liang, Y., Feng, J., Kim, J., Wang, H., Hong, G., Zhang, B. and Dai, H., "Advanced Zinc-air Batteries Based on High-performance Hybrid Electrocatalysts," *Nat. Comm.*, **4**, 1805(2013).
7. Grande, L., Paillard, E., Hassoun, J., Park, J. B., Lee, Y. J., et al., "The Lithium/Air Battery: Still an Emerging System or a Practical Reality?," *Adv. Mater.*, **27**, 784-800(2015).
8. Jung, H.-G., Hassoun, J., Park, J.-B., Sun, Y.-K. and Scrosati, B., "An Improved High-performance Lithium-Air Battery," *Nat. Chem.*, **4**, 579-585(2012).
9. Lee, J. S., Kim, S. T., Cao, R., Choi, N. S., Liu, M., et al., "Metal-Air Batteries with High Energy Density: Li-Air Versus Zn-Air," *Adv. Energ. Mater.*, **1**, 34-50(2012).
10. Caramia, V. and Bozzini, B., "Materials Science Aspects of Zinc-Air Batteries: a Review," *Materials for Renewable and Sustainable Energy*, **3**, 28(2014).
11. Hwang, H. J., Chi, W. S., Kwon, O., Lee, J. G., Kim, J. H. and Shul, Y.-G., "Selective Ion Transporting Polymerized Ionic Liquid Membrane Separator for Enhancing Cycle Stability and Durability in Secondary Zinc-Air Battery Systems," *ACS Appl. Mater. Interfaces*, **8**(39), 26298-26308(2016).

12. Liu, Y., Sun, Q., Li, W., Adair, K. R., Li, J. and Sun, X., "A Comprehensive Review on Recent Progress in Aluminum-Air Batteries," *Green Energy & Environment*, **2**, 246-277(2017).
13. Kwon, O., Hwang, H. J., Ji, Y., Jeon, O. S., Kim, J. P., Lee, C. and Shul, Y. G., "Transparent Bendable Secondary Zinc-Air Batteries by Controlled Void Ionic Separators," *Sci. Rep.*, **9**, 3175(2019).
14. Liu, Q., Chang, Z., Li, Z. and Zhang, X., "Flexible Metal-Air Batteries: Progress, Challenges, and Perspectives," *Small Methods*, **2**, 1700231(2018).
15. Zhang, T. and Zhou, H., "A Reversible Long-Life Lithium-Air Battery in Ambient Air," *Nat. Comm.*, **4**, 1817(2013).
16. Mainar, A. R., Iruin, E., Colmenares, L. C., Kvasha, A., Meatza, I., Bengoechea, M., Leonet, O., Boyano, I., Zhang, Z. and Blazquez, J. A., "An Overview of Progress in Electrolytes for Secondary Zinc-Air Batteries and Other Storage Systems Based on Zinc," *J. Energy Storage*, **15**, 304-328(2018).
17. Balaish, M., Kraytsberg, A. and Ein-Eli, Y., "A Critical Review on Lithium-Air Battery Electrolytes," *Phys. Chem. Chem. Phys.*, **16**, 2801-2822(2014).
18. Gelman, D., Shvartsev, B. and Ein-Eli, Y., "Aluminum-Air Battery Based on an Ionic Liquid Electrolyte," *J. Mater. Chem. A*, **2**, 20237-20242(2014).
19. Wang, Z.-L., Xu, D., Xu, J.-J. and Zhang, X.-B., "Oxygen Electrocatalysts in Metal-Air Batteries: from Aqueous to Nonaqueous Electrolytes," *Chem. Soc. Rev.*, **43**, 7746-7786(2014).
20. Li, Y., Gong, M., Liang, Y., Feng, J., Kim, J.-E., Wang, H., Hong, G., Zhang, B. and Dai, H., "Advanced Zinc-Air Batteries Based on High-Performance Hybrid Electrocatalysts," *Nat. Comm.,* **4**, 1805(2013).
21. Chen, Y., Ji, S., Zhao, S., Chen, W., Dong, J. and Cheong, W.-C., et al., "Enhanced Oxygen Reduction with Single-atomic-site Iron Catalysts for a Zinc-Air Battery And Hydrogen-Air Fuel Cell," *Nat. Comm.*, **9**, 5422(2018).
22. Chen, Z., Yu, A., Higgins, D., Li, H., Wang, H. and Chen, Z., "Highly Active and Durable Core-Corona Structured Bifunctional Catalyst for Rechargeable Metal-Air Battery Application," *Nano Lett.*, **12**, 1946-1952(2012).
23. Jung, K.-N., Hwang, S. M., Park, M.-S., Kim, K. J., Kim, J.-G., Dou, S. X., Kim, J. H. and Lee, J.-W., "One-dimensional Manganese-Cobalt Oxide Nanofibres As Bi-Functional Cathode Catalysts For Rechargeable Metal-Air Batteries," *Sci. Rep.*, **5**, 7665 (2014).
24. Miao, H., Wang, Z., Wang, Q., Sun, S., Xue, Y., Wang, F., Zhao, J., Liu, Z. and Yuan, J., "A New Family of Mn-Based Perovskite ($La_{1-x}Y_xMnO_3$) with Improved Oxygen Electrocatalytic Activity for Metal-air Batteries," *Energy*, **154**, 561-570(2018).
25. Li, Y., Xu, H., Chien, P. H., Wu, N., Xin, S., Xue, L., Park, K., Hu, Y. Y. and Goodenough, J. B., "A Perovskite Electrolyte That Is Stable in Moist Air for Lithium-Ion Batteries," *Angew. Chem., Int. Ed.*, **57**, 8587-8591(2018).
26. Anderson, H. U., Kuo, J. H. and Sparlin, D. M., "Review of Defect Chemistry of $LaMnO_3$ and $LaCrO_3$," *Proceedings of the Electrochemical Society*, PV **1989-19**, 3-14(1989).
27. Pena, M. A. and Fierro, J. L., "Chemical Structures and Performance of Perovskite Oxides," *Chem. Rev.,* **101**, 1981-2017(2001).
28. Voorhoeve, R. J. H., Johnson, D. W., Remeika, J. P. and Gallagher, P. K., "Perovskite Oxides: Materials Science in Catalysis," *Science*, **4**, 827-833(1977).
29. Karatzas, X., Jansson, K., González, A., Dawody, J., Svensson, A. and Pettersson, L., "Zone-coated Rh-based Monolithic Catalyst for Autothermal Reforming of Diesel," *Appl. Catal. B-Environ.,* **101**, 226-238(2011).
30. Chervin, C. N., Long, J. W., Brandel, N. L., Wallace, J. M., Kuck, N. W. and Roliso, D. R., "Redesigning Air Cathodes for Metal-air Batteries Using MnOx-functionalized Carbon Nanofoam Architectures," *J. Power Sources,* **207**, 191-198(2012).
31. Jeon, Y., Park, D. H., Park, J. I., Yoon, S. H., Mochida, I., Choy, J. H. and Shul, Y. G., "Hollow Fibers Networked with Perovskite Nanoparticles for H_2 Production from Heavy Oil," *Sci. Rep.,* **3**, 2902(2013).
32. Jeon, Y., Lee, C., Rhee, J., Lee, G., Myung, J. H., Park, M., Park, J. I., Einaga, H. and Shul, Y. G., "Autothermal Reforming of Heavy-hydrocarbon Fuels by Morphology Controlled Perovskite Catalysts Using Carbon Templates," *Fuel* **187**, 446-456(2017).
33. Jeon, Y., Myung, J.-H., Hyun, S.-H., Shul, Y.-G. and Irvine, J. T. S., "Corn-cob Like Nanofibres as Cathode Catalysts for an Effective Microstructure Design in Solid Oxide Fuel Cells," *J. Mater. Chem. A*, **5**, 3966-3973(2017).
34. Jeon, Y., Ji, Y., Cho, Y.I., Lee, C., Park, D.-H. and Shul, Y.-G., "Oxide-Carbon Nanofibrous Composite Support for a Highly Active and Stable Polymer Electrolyte Membrane Fuel-Cell Catalyst," *ACS Nano*, **12**, 6819-6829(2018).
35. Sunarso, J., Torriero, A. A. J., Zhou, W., Howlett, P. C. and Forsyth, M., "Oxygen Reduction Reaction Activity of La-Based Perovskite Oxides in Alkaline Medium: A Thin-Film Rotating Ring-Disk Electrode Study," *J. Phys. Chem. C*, **116**, 5827(2012).
36. Cazaux, J., "Mechanisms of Charging in Electron Spectroscopy," *J. Electron Spectrosc. Relat. Phenom.,* **105**, 155(1999).
37. Palina, N., Wang, L., Dash, S., Yu, X., Breese, M. B. H., Wang, J. and Rusydi, A., "Investigation of the Metal-insulator Transition in $NdNiO_3$ Films by Site-selective X-ray Absorption Spectroscopy," *Nanoscale*, **9**, 6094-6102(2017).
38. Gilbert, B., Andres, R., Perfetti, P., Margaritondo, G., Rempfer, G. and de Stasio, G., "Charging Phenomena in PEEM Imaging and Spectroscopy," *Ultramicroscopy*, **83**, 129-39(2000).
39. Harano, T., Shibata, G., Ishigami, K., Takashashi, Y., Verma, V. K., Singh, V. R., et al., "Role of Doped Ru in Coercivity-enhanced $La_{0.6}Sr_{0.4}MnO_3$ Thin Film Studied by X-ray Magnetic Circular Dichroism," *Appl. Phys. Lett.*, **102**, 222404(2013).
40. Masuda, Y., Hosokawa, S. and Inoue, M., "Combustion Activities of the Ru Catalysts Supported on Hexagonal $YbFeO_3$," *J. Ceram. Soc. Jpn.*, **119**, 850-854(2011).